Visibility Interpolation in Solar Hard X-Ray Imaging: Application to RHESSI and STIX

The Astrophysical Journal, 919:133 (12pp), 2021 October 1 https://doi.org/10.3847/1538-4357/ac158d

Visibility Interpolation in Solar Hard X-Ray Imaging: Application to RHESSI and STIX

Emma Perracchione[1], Paolo Massa[2], Anna Maria Massone[1], and Michele Piana[1]
[1] Dipartimento di Matematica, Università di Genova and CNR—SPIN Genova, Genova, Italy; piana@dima.unige.it
[2] Dipartimento di Matematica, Università di Genova, Genova, Italy
Received 2021 March 29; revised 2021 July 16; accepted 2021 July 17; published 2021 October 4

Abstract

Space telescopes for solar hard X-ray imaging provide observations made of sampled Fourier components of the incoming photon flux. The aim of this study is to design an image reconstruction method relying on enhanced visibility interpolation in the Fourier domain. The interpolation-based method is applied to synthetic visibilities generated by means of the simulation software implemented within the framework of the Spectrometer/Telescope for Imaging X-rays (STIX) mission on board Solar Orbiter. An application to experimental visibilities observed by the Reuven Ramaty High Energy Solar Spectroscopic Imager (RHESSI) is also considered. In order to interpolate these visibility data, we have utilized an approach based on Variably Scaled Kernels (VSKs), which are able to realize feature augmentation by exploiting prior information on the flaring source and which are used here, for the first time, in the context of inverse problems. When compared to an interpolation-based reconstruction algorithm previously introduced for RHESSI, VSKs offer significantly better performance, particularly in the case of STIX imaging, which is characterized by a notably sparse sampling of the Fourier domain. In the case of RHESSI data, this novel approach is particularly reliable when the flaring sources are either characterized by narrow, ribbon-like shapes or high-resolution detectors are utilized for observations. The use of VSKs for interpolating hard X-ray visibilities allows remarkable image reconstruction accuracy when the information on the flaring source is encoded by a small set of scattered Fourier data and when the visibility surface is affected by significant oscillations in the frequency domain.

Unified Astronomy Thesaurus concepts: Solar x-ray flares (1816); X-ray telescopes (1825); Astronomy data analysis (1858)

1. Introduction

The inversion of the Fourier transform from limited data is a well-known problem in several imaging domains like, for instance, medical imaging (McGibney et al. 1993; Bronstein et al. 2002; Sutton et al. 2003; Fessler 2007; Gallagher et al. 2008; Lustig et al. 2008), crystallography (Eisebitt et al. 2004; Marchesini et al. 2008; Brady et al. 2009), and geophysics (Brossier et al. 2009; Jin 2010). This image reconstruction problem inspired several computational approaches like nonuniform Fast Fourier Transform (FFT) (Bronstein et al. 2002; Fessler & Sutton 2003; Greengard & Lee 2004; Lee & Greengard 2005), compressed sensing (Donoho 2006; Lustig et al. 2008; Bigot et al. 2016), and machine learning (Wang et al. 2018; Ravishankar et al. 2019). In the case of astronomical imaging, the use of Fourier methods is mainly related to radio and optical interferometry (Le Besnerais et al. 2008; Thiébaut & Giovannelli 2009; Wiaux et al. 2009; Felli & Spencer 2012; Thompson et al. 2017; Ye et al. 2020), although a similar methodology also involves snapshot imaging spectroscopy (Culhane et al. 2007; Harra et al. 2017; Courrier & Kankelborg 2018; Winebarger et al. 2019). However, in the last three decades, this approach has been utilized also in the case of solar hard X-ray telescopes that have been conceived in order to provide spatial Fourier components of the photon flux emitted via either the bremsstrahlung or thermal processes during solar flares (Lin et al. 2002; Krucker et al. 2020). These Fourier components, named visibilities, are sampled by the hard X-ray instrument in the two-dimensional Fourier space, named the (u, v) plane, in a sparse way, according to a geometry dependent on the instrument design. For instance, NASA's Reuven Ramaty High Energy Spectroscopic Imager (RHESSI) relies on the use of a set of nine Rotating Modulation Collimators (RMCs) whose FWHM is logarithmically spaced between 2.″3 and 183″ (Hurford et al. 2002). Each RMC measures visibilities on a circle of points in the (u, v) space with a spatial frequency that corresponds to its angular resolution and a position angle that varies according to the spacecraft rotation (see Figure 1, left panel). On the other hand, the Spectrometer/Telescope for Imaging X-rays (STIX) on board ESA's Solar Orbiter is based on the Moiré pattern technology (Giordano et al. 2015; Massa et al. 2019), and its 30 collimators sample the (u, v) plane over a set of six spirals for an FWHM resolution coarser than 7″ (see Figure 1, right panel).

Both RHESSI and, even more significantly, STIX measure very few Fourier components and often with a rather limited signal-to-noise ratio. This notable sparsity of the sampling in the Fourier domain explains why the methods designed for other Fourier-based applications do not properly work in this case. For instance, in RHESSI the optimum number of visibilities imposed by the Shannon theorem should be around 300, while the number of statistically significant visibilities provided by an observation of the NASA satellite is just a few dozen. By contrast, solar interferometry typically produces several thousands of independent visibilities, all with high signal-to-noise ratios, and, as a result, the gridding-based reconstruction methods designed for this modality cannot be successfully applied in hard X-ray-visibility-based imaging. The image reconstruction problem in solar hard X-ray imaging is more severely ill posed than other Fourier-based imaging problems in which the direct computation of the inverse discrete Fourier Transform, for example, by means of nonuniform FFT algorithms, provides reliable results. As a confirmation of this, the computation of the inverse discretized Fourier Transform of RHESSI visibilities leads to reconstructions affected by a notable quantity of artifacts and therefore of limited use for physical investigation (see the back-projections in the RHESSI

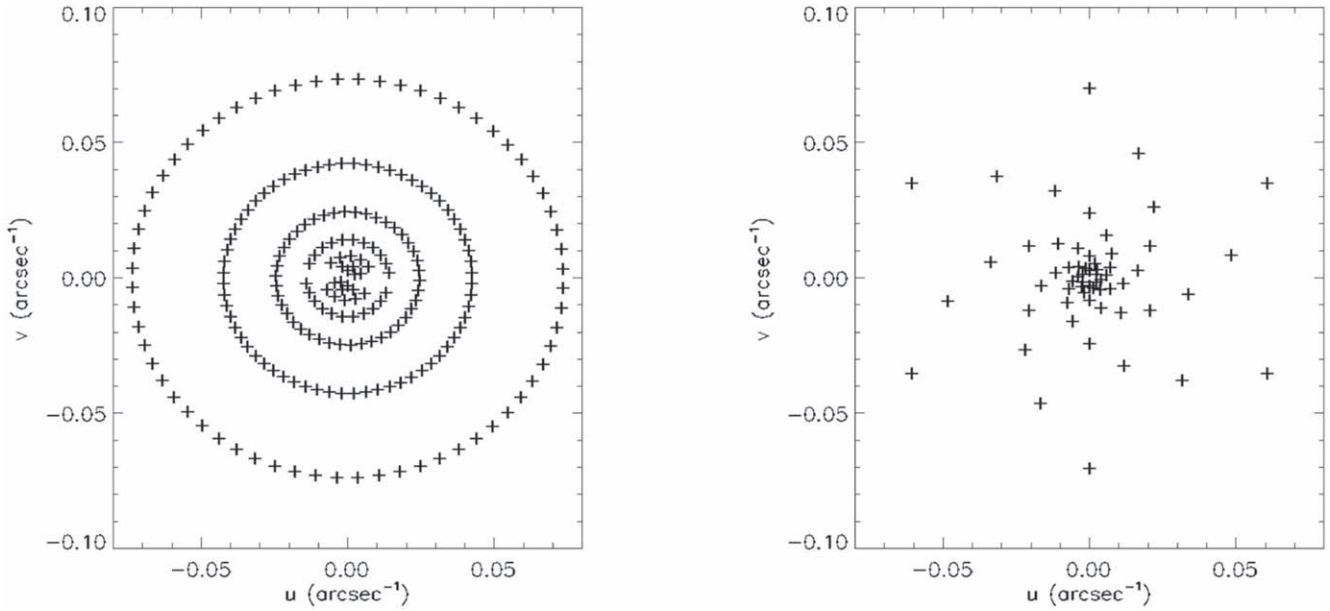

Figure 1. The sampling of the (u, v) plane provided by RHESSI (left panel) and STIX (right panel).

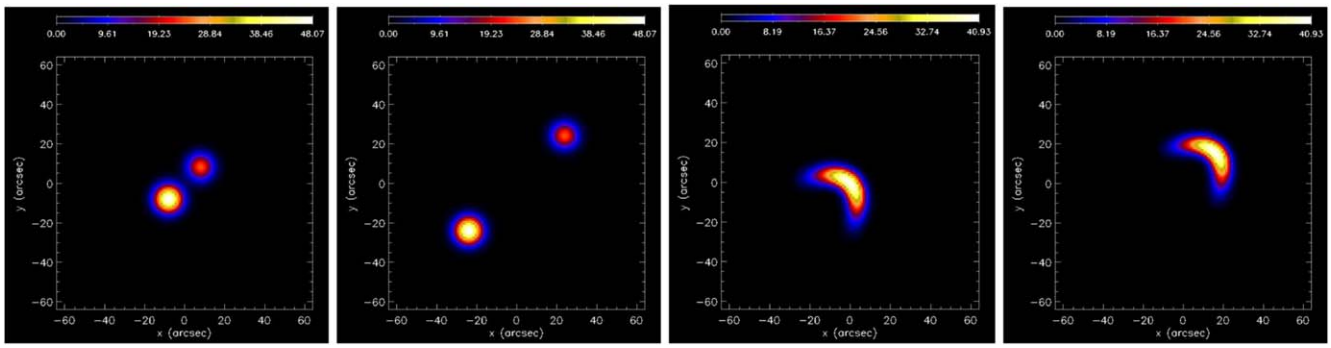

Figure 2. Ground-truth configurations.

image archive at https://hesperia.gsfc.nasa.gov/rhessi_extras/flare_images/hsi_flare_image_archive.html).

Therefore, image reconstruction methods in solar hard X-ray astronomy rely on procedures that allow some sort of interpolation/extrapolation in the (u, v) space in order to recover information in between the sampled frequencies to reduce the imaging artifacts and, outside the sampling domain, to obtain superresolution effects. Most methods accomplish these objectives by imposing constraints in the image domain, either by optimizing parameters associated with predefined image shapes via comparison with observations (Aschwanden et al. 2002; Sciacchitano et al. 2018) or by minimizing regularization functionals that combine a fitting term with a stability term (Felix et al. 2017; Duval-Poo et al. 2018; Massa et al. 2020).

However, the most straightforward approach to interpolation/extrapolation in visibility-based imaging is probably the one implemented in the uv_smooth method (Massone et al. 2009), which is inspired by standard gridding approaches utilized in radio astronomy. In particular, uv_smooth starts from the observation that the coverage of the (u, v) plane offered by hard X-ray instruments is much sparser than that typical in radio astronomy and therefore utilizes spline interpolation at spatial frequencies smaller than the largest sampled frequencies and soft-thresholding on the image to reduce the ringing effects due to a naive and unconstrained Fourier transform inversion procedure (Daubechies et al. 2004; Allavena et al. 2012). This approach can exploit FFT in the inversion process and is characterized by satisfactory reliability when reconstructing extended sources (Guo et al. 2013; Caspi et al. 2015); however, several applications (Bonettini & Prato 2014; Dennis & Tolbert 2019) showed that uv_smooth does not work properly when it is applied to visibility sets characterized by significant oscillations in the (u, v) plane. This misbehavior is essentially due to the fact that the interpolation algorithm utilized in uv_smooth is not optimal and often misses the oscillating frequency information related to very narrow or well-separated sources (or, in the case of RHESSI, associated with the use of detectors with fine grids in the observation process).

The present paper proposes an enhanced release of uv_smooth, based on the use of an advanced approach to interpolation in the frequency domain. Specifically, this approach relies on the use of Variably Scaled Kernels (VSKs), which are able to include a priori information in the interpolation process (Bozzini et al. 2015; De Marchi et al. 2020a; Campagna & Perracchione 2021). This additional knowledge is implicitly put into the kernel via a scaling function that determines the accuracy of the approximation process and that is linked to a first coarse reconstruction of the sought image. As far as the practical implementation of the VSK setting is concerned, in this study, we considered the Matérn C^0

Table 1
Results for the Reconstruction of Configuration 1

	First Peak			
	x_p	y_p	FWHM	FLUX ($\times 10^3$)
Simulated	−8.0	−8.0	11.0	6.58
uv_smooth	-6.0 ± 0.6	-5.0 ± 0.4	11.2 ± 0.3	5.08 ± 0.13
uv_smooth_BP	-6.3 ± 0.4	-6.2 ± 0.4	11.5 ± 0.4	5.53 ± 0.13
uv_smooth_CC	-7.0 ± 1.9	-6.8 ± 1.8	14.5 ± 7.0	5.98 ± 0.95
CLEAN	-8.0 ± 0.5	-7.1 ± 0.4	9.51 ± 0.5	5.73 ± 0.11
Forward fit	-7.8 ± 0.4	-7.9 ± 0.4	11.8 ± 1.3	6.55 ± 0.36
	Second Peak			
	x_p	y_p	FWHM	FLUX ($\times 10^3$)
Simulated	8.0	8.0	11.0	3.21
uv_smooth	8.0 ± 0.5	6.4 ± 0.5	10.7 ± 0.5	2.42 ± 0.12
uv_smooth_BP	8.1 ± 0.4	8.3 ± 0.6	11.5 ± 0.5	2.70 ± 0.13
uv_smooth_CC	7.9 ± 0.6	6.9 ± 0.3	12.3 ± 0.8	2.77 ± 0.14
CLEAN	8.3 ± 0.4	6.3 ± 1.4	10.3 ± 1.0	2.50 ± 0.16
Forward fit	7.9 ± 0.6	7.9 ± 0.4	10.8 ± 1.8	3.08 ± 0.54
				Total Flux ($\times 10^3$)
Simulated				10.00
uv_smooth				9.27 ± 0.18
uv_smooth_BP				9.86 ± 0.23
uv_smooth_CC				10.10 ± 0.19
CLEAN				8.72 ± 0.06
Forward fit				9.63 ± 0.77

Note. The footpoint centers are denoted as (x_p, y_p) while the flux is measured in photons cm^{-2} s^{-1}.

Table 2
Results for the Reconstruction of Configuration 2

	First Peak			
	x_p	y_p	FWHM	FLUX ($\times 10^3$)
Simulated	−24.0	−24.0	11.0	6.51
uv_smooth	-7.5 ± 0.5	-10.6 ± 0.4	8.05 ± 0.1	2.41 ± 0.19
uv_smooth_BP	-21.9 ± 0.2	-21.7 ± 0.4	10.8 ± 0.2	5.26 ± 0.11
uv_smooth_CC	-21.8 ± 0.3	-21.7 ± 0.4	11.4 ± 0.4	5.27 ± 0.12
CLEAN	-23.5 ± 0.4	-22.8 ± 0.3	9.98 ± 0.8	5.39 ± 0.11
Forward fit	-24.1 ± 0.2	-23.9 ± 0.1	11.3 ± 0.8	6.31 ± 0.29
	Second Peak			
	x_p	y_p	FWHM	FLUX ($\times 10^3$)
Simulated	24.0	24.0	11.0	3.25
uv_smooth	8.5 ± 0.5	-9.4 ± 0.8	9.50 ± 0.1	1.28 ± 0.26
uv_smooth_BP	24.0 ± 0.2	24.4 ± 0.5	10.9 ± 0.2	2.50 ± 0.12
uv_smooth_CC	23.3 ± 0.3	24.6 ± 0.8	10.9 ± 0.7	2.35 ± 0.14
CLEAN	23.8 ± 0.3	22.8 ± 0.4	10.8 ± 0.8	2.24 ± 0.12
Forward fit	23.9 ± 0.5	23.8 ± 0.5	11.6 ± 1.9	3.17 ± 0.10
				Total Flux ($\times 10^3$)
Simulated				10.00
uv_smooth				9.88 ± 0.34
uv_smooth_BP				10.55 ± 0.30
uv_smooth_CC				12.37 ± 0.28
CLEAN				9.96 ± 0.64
Forward fit				9.47 ± 0.29

Note. The footpoint centers are denoted as (x_p, y_p) while the flux is measured in photons cm^{-2} s^{-1}.

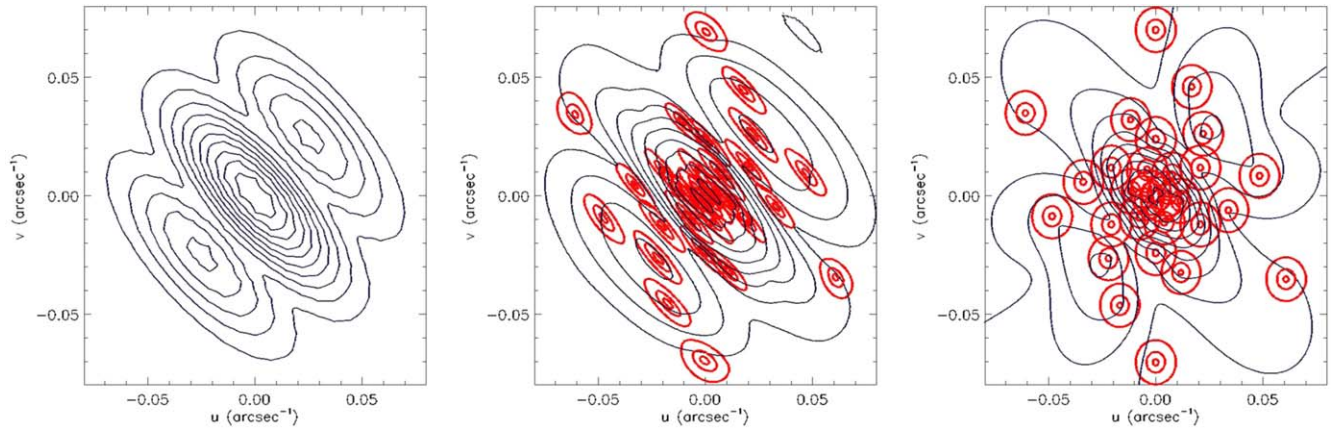

Figure 3. First panel: contour levels of the modulus of the ground-truth visibility surfaces for Configuration 1. Second and third panels: the contour levels of the modulus of the visibility surfaces reconstructed by uv_smooth_BP and uv_smooth with the associated basis functions (red).

Table 3
Results for the Reconstruction of Configuration 3

	x_p	y_p	Total Flux ($\times 10^3$)
Simulated	0.0	0.0	10.00
uv_smooth	0.7 ± 0.6	1.3 ± 0.5	9.71 ± 0.27
uv_smooth_BP	-0.5 ± 0.6	1.4 ± 0.6	10.55 ± 0.02
uv_smooth_CC	-0.6 ± 0.5	0.6 ± 0.4	10.55 ± 0.02
CLEAN	0.1 ± 0.9	0.2 ± 0.8	8.79 ± 0.11

Note. The position of the pixel with maximum intensity is denoted as (x_p, y_p). The flux units are photons cm^{-2} s^{-1}.

Table 4
Results for the Reconstruction of Configuration 4

	x_p	y_p	Total Flux ($\times 10^3$)
Simulated	18.0	18.0	10.00
uv_smooth	15.4 ± 0.8	11.4 ± 0.7	9.78 ± 0.32
uv_smooth_BP	16.6 ± 0.7	15.8 ± 0.8	10.41 ± 0.02
uv_smooth_CC	17.0 ± 0.7	16.8 ± 0.8	10.59 ± 0.01
CLEAN	18.8 ± 0.5	17.5 ± 0.8	8.91 ± 0.08

Note. The position of the pixel with maximum intensity is denoted as (x_p, y_p). The flux units are photons cm^{-2} s^{-1}.

kernel, which takes advantage of a low-regularity degree and of a better numerical stability (Matérn 1986).

The plan of the paper is as follows. Section 2 illustrates the interpolation process based on VSKs. Section 3 describes the overall image reconstruction approach relying on the use of interpolation in the (u, v) plane and of the soft-thresholding technique applied for image reconstruction. Section 4 contains some validation tests performed against both synthetic STIX visibilities and experimental RHESSI observations. Our conclusions are offered in Section 5.

2. Interpolation in the Fourier Domain

Visibility-based hard X-ray telescopes provide experimental measurements of the Fourier transform of the incoming photon flux at specific points of the spatial frequency plane. We denote with $\boldsymbol{f}$ the vector whose components are the discretized values of the incoming flux, with $\boldsymbol{F}$ the discretized Fourier transform sampled at the set of points $\{\boldsymbol{u}_i = (u_i, v_i)\}_{i=1}^{n}$ in the (u, v) plane and with $\boldsymbol{V}$ the vector whose n components are the observed visibilities. Then, the image formation model in this framework can be approximated by

$$\boldsymbol{V} = \boldsymbol{F}\boldsymbol{f} \ . \tag{1}$$

The uv_smooth code incorporated in the SSW tree and validated in the case of RHESSI visibilities addresses Equation (1) by means of an interpolation/extrapolation procedure in which the interpolation step is carried out via an algorithm based on spline functions and the extrapolation step is realized by means of a soft-thresholding scheme (Daubechies et al. 2004; Allavena et al. 2012). In the present paper, we want to generalize the interpolation step of uv_smooth by means of a more sophisticated numerical technique in order to improve uv_smooth performance, particularly in the case when visibility oscillations are significant.

In general, any interpolation approach seeks a function, namely P, that matches the given measurements at their corresponding locations. Thus, an interpolant of the visibilities is constructed in such a way that

$$P(\boldsymbol{u}_i) = \boldsymbol{V}_i, \quad i = 1,\ldots,n. \tag{2}$$

Typically, any interpolating function is of the form

$$P(\boldsymbol{u}) = \sum_{k=1}^{n} a_k b_k(\boldsymbol{u}) \ , \tag{3}$$

where $\{b_1(\boldsymbol{u}),\ldots,b_n(\boldsymbol{u})\}$ is a set of appropriate basis functions and $\boldsymbol{u}$ is a vector in the interpolation domain. A possible choice for these basis functions is represented by the so-called radial basis functions (RBFs); see, e.g (Fasshauer 2007), which have the property that

$$b_k(\boldsymbol{u}) = \phi(\|\boldsymbol{u} - \boldsymbol{u}_k\|), \quad k = 1,\ldots,n \ , \tag{4}$$

where ϕ is a specific RBF and $\|\cdot\|$ denotes the Euclidean norm. In order to incorporate possible prior information in the interpolation process, the VSKs represent an alternative choice with respect to RBFs, in which

$$b_k(\boldsymbol{u}) = \phi(\|(\boldsymbol{u}, \psi(\boldsymbol{u})) - (\boldsymbol{u}_k, \psi(\boldsymbol{u}_k))\|), \quad k = 1,\ldots,n \ , \tag{5}$$

and where ψ is the so-called scaling function encoding such prior information on the emitting source $\boldsymbol{f}$. In the following, we will choose ψ: $\mathbb{R}^2 \to \mathbb{R}^2$, and therefore, $(\boldsymbol{u}, \psi(\boldsymbol{u}))$ and $(\boldsymbol{u}_k, \psi(\boldsymbol{u}_k))$ are two row vectors obtained by concatenating $\boldsymbol{u}$, $\psi(\boldsymbol{u})$ and $\boldsymbol{u}_k$, $\psi(\boldsymbol{u}_k)$, respectively.

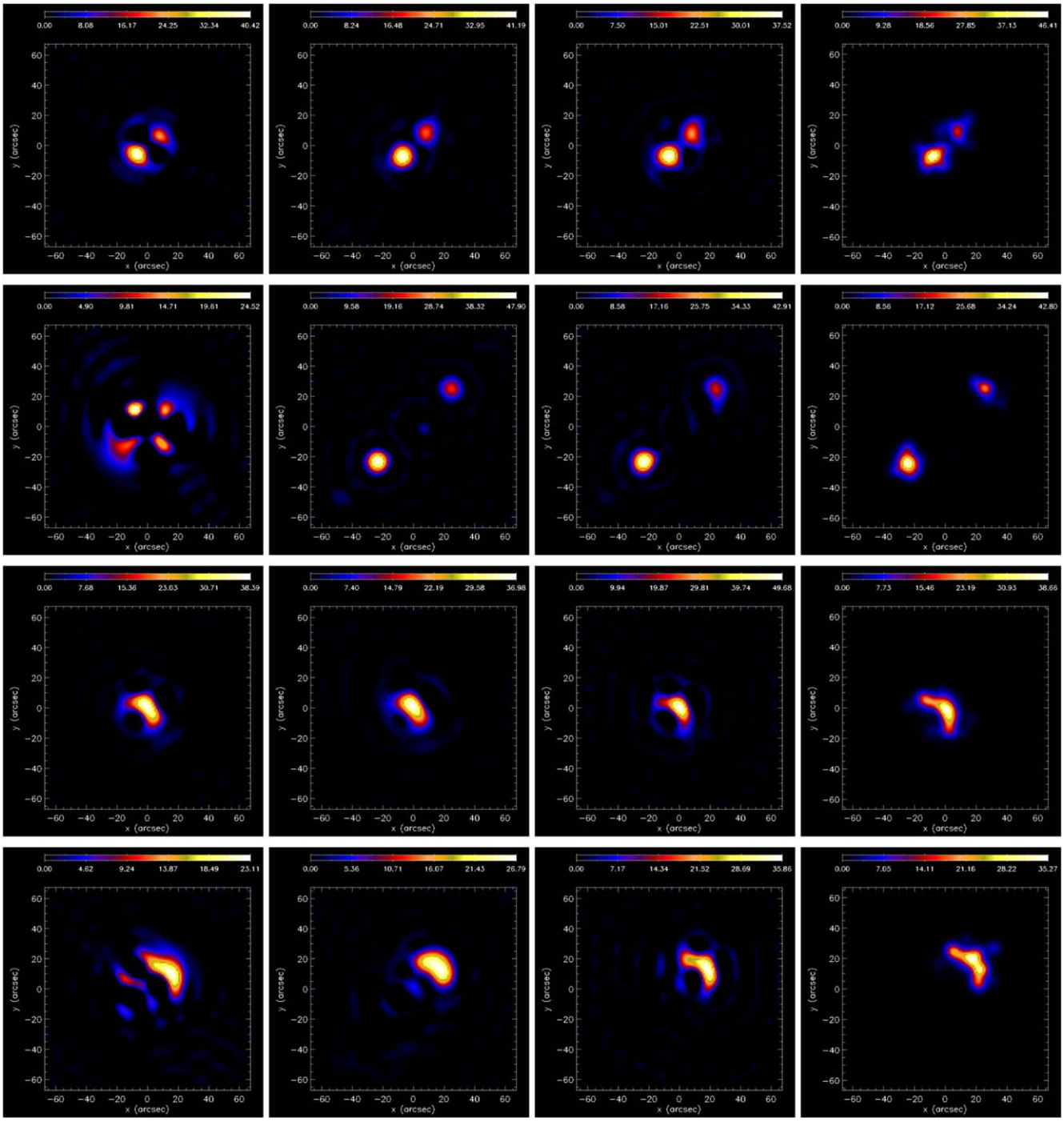

Figure 4. Reconstructions of four synthetic flaring configurations using simulated STIX visibilities. First column: reconstructions provided by uv_smooth. Second column: reconstructions obtained by using VSK-based interpolation when ψ is based upon the back-projected map (uv_smooth_BP). Third column: reconstructions obtained by using VSK-based interpolation when ψ is based upon the map of the CLEAN components (uv_smooth_CC). Fourth column: reconstructions obtained by using CLEAN. The ground-truth and reconstruction parameter values are in Tables 1–4.

Therefore, once the functions ϕ and ψ are chosen, by imposing conditions (2), the interpolation problem is reduced to the solution of the linear system

$$K\boldsymbol{a} = \boldsymbol{V}\ , \tag{6}$$

where $\boldsymbol{a} = (a_1,\ldots,a_n)^T$, $\boldsymbol{V} = (\boldsymbol{V}_1,\ldots,\boldsymbol{V}_n)^T$, and $K_{ij} = \phi(\|(\boldsymbol{u}_i, \psi(\boldsymbol{u}_i)) - (\boldsymbol{u}_j, \psi(\boldsymbol{u}_j))\|)$, $i, j = 1,\ldots, n$. Once system (6) is solved, the computed vector $\boldsymbol{a}$ is used to evaluate the interpolating function $P(\boldsymbol{u})$ on N^2 points $\{\overline{\boldsymbol{u}}_1,\ldots,\overline{\boldsymbol{u}}_{N^2}\}$ of a regular mesh of the (u, v) plane, with $N^2 \gg n$. This provides the visibility surface $\overline{\boldsymbol{V}}$ such that

$$\overline{\boldsymbol{V}}_k = P(\overline{\boldsymbol{u}}_k) = \sum_{i=1}^{n} a_i \phi(\|(\overline{\boldsymbol{u}}_k, \psi(\overline{\boldsymbol{u}}_k)) - (\boldsymbol{u}_i, \psi(\boldsymbol{u}_i))\|), \tag{7}$$

for $k = 1,\ldots, N^2$. Once the interpolated visibility surface $\overline{\boldsymbol{V}}$ has been computed, the image reconstruction problem becomes

$$\overline{\boldsymbol{V}} = \overline{\boldsymbol{F}}\boldsymbol{f}\ , \tag{8}$$

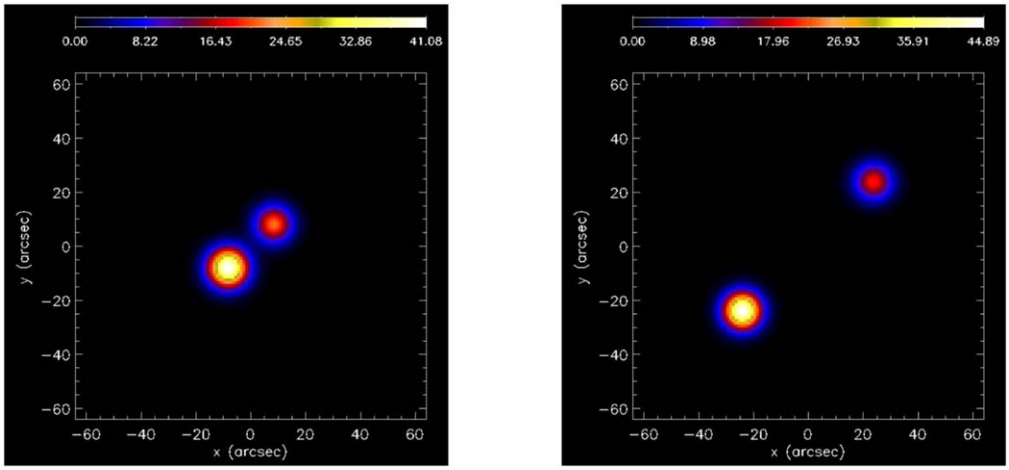

Figure 5. Left to right: reconstructions provided by a forward-fit algorithm for Configurations 1 and 2, respectively.

Table 5
CPU Burden (in Seconds) Employed by the Three Reconstruction Algorithms Averaged over the Data Corresponding to the Four Configurations

	CPU times
uv_smooth	0.18
uv_smooth_BP	4.24
uv_smooth_CC	6.78
CLEAN	2.34

where $\overline{\boldsymbol{F}}$ is the $N^2 \times N^2$ discretized Fourier transform and $\overline{\boldsymbol{f}}$ is the $N^2 \times 1$ vector to reconstruct.

Some comments are relevant to the conclusion of this section.

First, as far as the choice of the scaling function ψ in Equation (7) is concerned, our strategy consists of computing a rough approximation of the sought image as a first step. Once this approximation is determined, the second step is to construct the scaling function ψ as its discretized Fourier transform. More formally, if $\tilde{\boldsymbol{f}}$ is the $N^2 \times 1$ vector representing the approximation and $\tilde{\boldsymbol{V}} = \overline{\boldsymbol{F}}\tilde{\boldsymbol{f}}$ is its corresponding discretized Fourier transform, then the scaling function is the function ψ: $\mathbb{R}^2 \to \mathbb{R}^2$ such that $\psi(\overline{\boldsymbol{u}}_k) = \tilde{\boldsymbol{V}}(\overline{\boldsymbol{u}}_k) = (\mathrm{Re}(\tilde{V}(\overline{\boldsymbol{u}}_k)), \mathrm{Im}(\tilde{V}(\overline{\boldsymbol{u}}_k))) \in \mathbb{R}^2$, $k = 1,\ldots, N^2$. In the applications considered in this paper we have followed two different ways of construction of the scaling function:

1. In one approach, the approximated solution $\tilde{\boldsymbol{f}}$ is obtained by applying the back-projection algorithm to the measured visibilities and by thresholding the back-projected map in order to account for the most significant part of the signal and for a rough estimate of the source position.
2. In the other approach, $\tilde{\boldsymbol{f}}$ is simply given by the map of the CLEAN components provided as an intermediate step by the CLEAN algorithm.

The second comment is that, from a technical viewpoint, the choice of ϕ should guarantee the numerical stability of system (6), while the selection of ψ should encode a priori information on the flaring source. Therefore, concerning the basis function, we took the Matérn C^0 kernel (Matérn 1986), defined as

$$\phi(||\boldsymbol{u}||) = \mathrm{e}^{-\varepsilon||\boldsymbol{u}||}, \tag{9}$$

where ε is the so-called shape parameter. This RBF takes advantage of a low regularity (indeed it is C^0), and hence it usually prevents numerical instability, which also grows according to the regularity of the basis function. Moreover, at a more general level, VSK approaches map the original measured data into a higher dimension space and therefore can be considered as a feature augmentation strategy. It follows that the definition of the scaling function ψ plays a crucial role in the final outcome of this approach and the idea is to select it so that it mimics the measured samples as shown in Romani et al. (2019) and De Marchi et al. (2020a, 2020b).

Finally, in several conditions, flaring sources can be realistically mimicked by rather compact sources in the image space, which reflects in smooth visibility surfaces in the Fourier domain. Therefore, the use of RBFs in this context is appropriate, because these basis functions do not have compact support. Moreover, the Matérn kernel shows the following inverse Fourier decay:

$$\check{\phi}(\boldsymbol{x}) \propto (\varepsilon^2 + ||\boldsymbol{x}||)^{-\beta}, \quad \beta = \frac{d+1}{2}, \tag{10}$$

where d denotes the space dimension. Such a formula implies that for small values of the shape parameter, the inverse Fourier transform decays very rapidly. And, as the visibility surfaces are a linear combination of Matérn functions, selecting small values for the shape parameter allows us to mimic compact sources in the physical domain. From an operational viewpoint, the parameter ε has been determined according to the approach described by De Marchi et al. (2005), with the resulting value $\varepsilon = 0.001$.

3. Image Reconstruction

The implementation of an image reconstruction process relying on the interpolation procedure described in the previous section needs the definition of a pipeline made of the following steps:

1. Construction of the matrix K. This step needs the choice of the function ϕ generating the RBF (see Equation (9)) and of the scaling function ψ, which implies accounting for some prior information on the source image. As far as ψ is concerned, as said in the previous section in this study, we have implemented two possible choices, based on coarse estimates of the X-ray source to reconstruct,

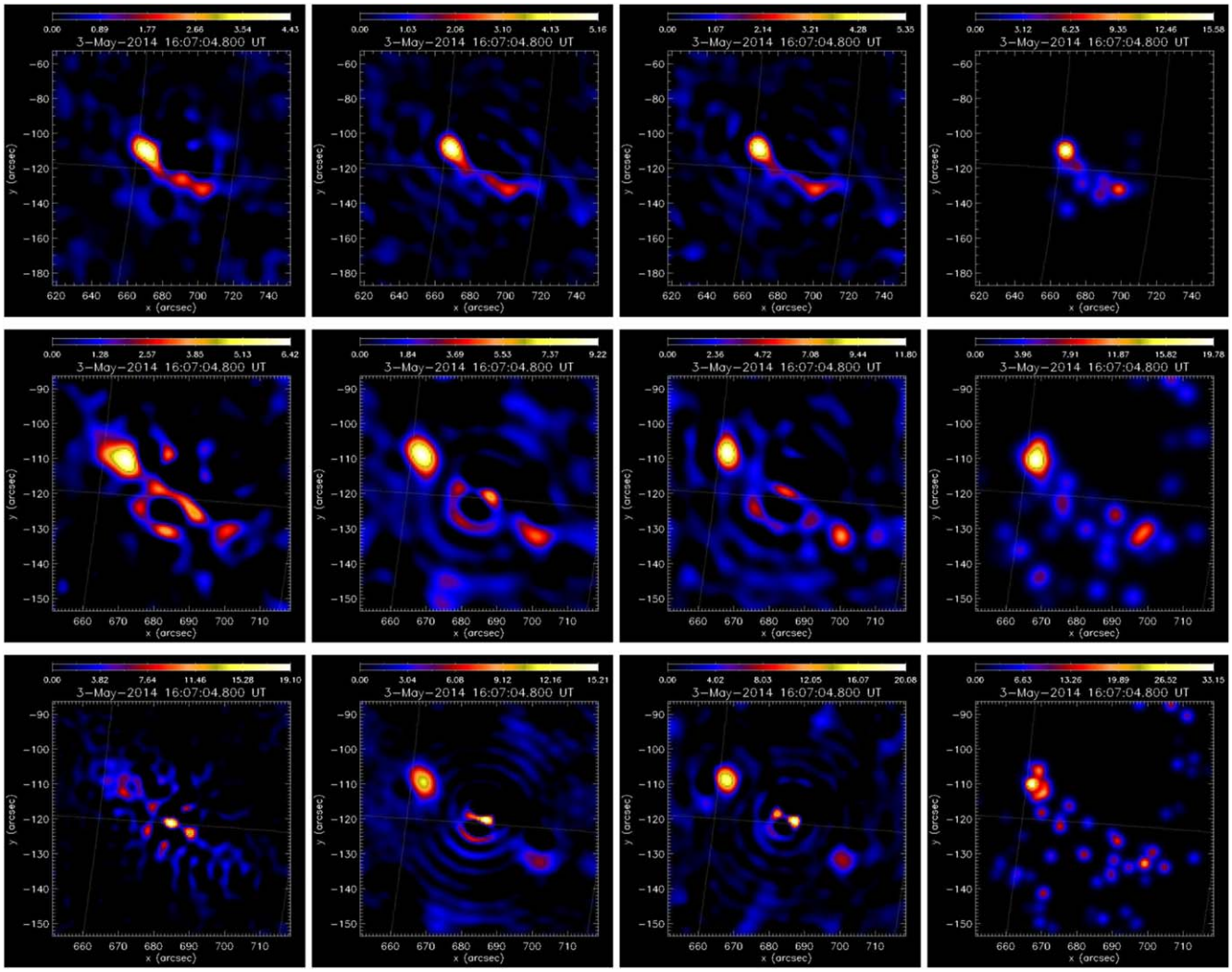

Figure 6. Reconstruction of the flare observed by RHESSI on 2014 May 3 at 16:07:04 UT. From left to right, the columns contain the reconstructions via uv_smooth, uv_smooth_BP, uv_smooth_CC, and CLEAN. From top to bottom the three rows indicate the reconstructions obtained using RHESSI detectors 3 through 9, 2 through 9, and 1 through 9, respectively.

i.e., the Fourier transforms of the back-projected map and of the map of the CLEAN components, respectively. Note that the main information returned by both maps is the maximum value of the sought image, which roughly represents the most intense peak. In particular, the CLEAN component map, before being convolved with an idealized PSF, identifies the most intense pixels starting from the back-projected map.

2. Solution of Equation (6). This is a square and rather well-conditioned linear system, and therefore, standard numerics for computing K^{-1} works properly in the case of input data characterized by large signal-to-noise ratios. When the data statistics is low, the system is solved by means of the equally standard Tikhonov method (Massone et al. 2003). Such regularization provides an approximation of the exact solution of Equation (6) that realizes a tradeoff between smoothing and fitting; see Fasshauer & McCourt (2015, Section 15).
3. Reconstruction of the image $\overline{f}$ starting from the $\overline{V}$ returned by the interpolation procedure. We perform a zero-padding strategy, as in the standard implementation of uv_smooth, and we then subsample such an image to obtain an $M \times M$ grid, with $M = 128$. Then, we have implemented a soft-thresholding approach based on the projected Landweber iterative scheme (Piana & Bertero 1996, 1997):

$$\overline{f}^{(k+1)} = \mathcal{P}_+[\overline{f}^{(k)} + \overline{F}^T(\overline{V} - \overline{F}\overline{f}^{(k)})]\,, \tag{11}$$

where $\mathcal{P}_+$ imposes a positivity constraint pixel-wise, i.e., it returns zero for each negative pixel value. In the present implementation, we have assumed the initialization $\overline{f} = 0$ and a stopping rule that relies on a check on the χ^2 values (Allavena et al. 2012).

There are essentially two main advantages of this scheme. First, the positivity constraint induces superresolution effects because it allows the frequency information outside the support of the interpolated visibility surface to be extrapolated (Piana & Bertero 1996). Second, the computational burden of the iterative scheme (11) is reduced if one utilizes the FFT routine to compute the direct and inverse Fourier transforms.

As a final remark for this section, we point out that the two choices we indicated for the scaling functions ψ are not the only ones possible, and other candidate functions may realize feature augmentation as well. However, both choices can be

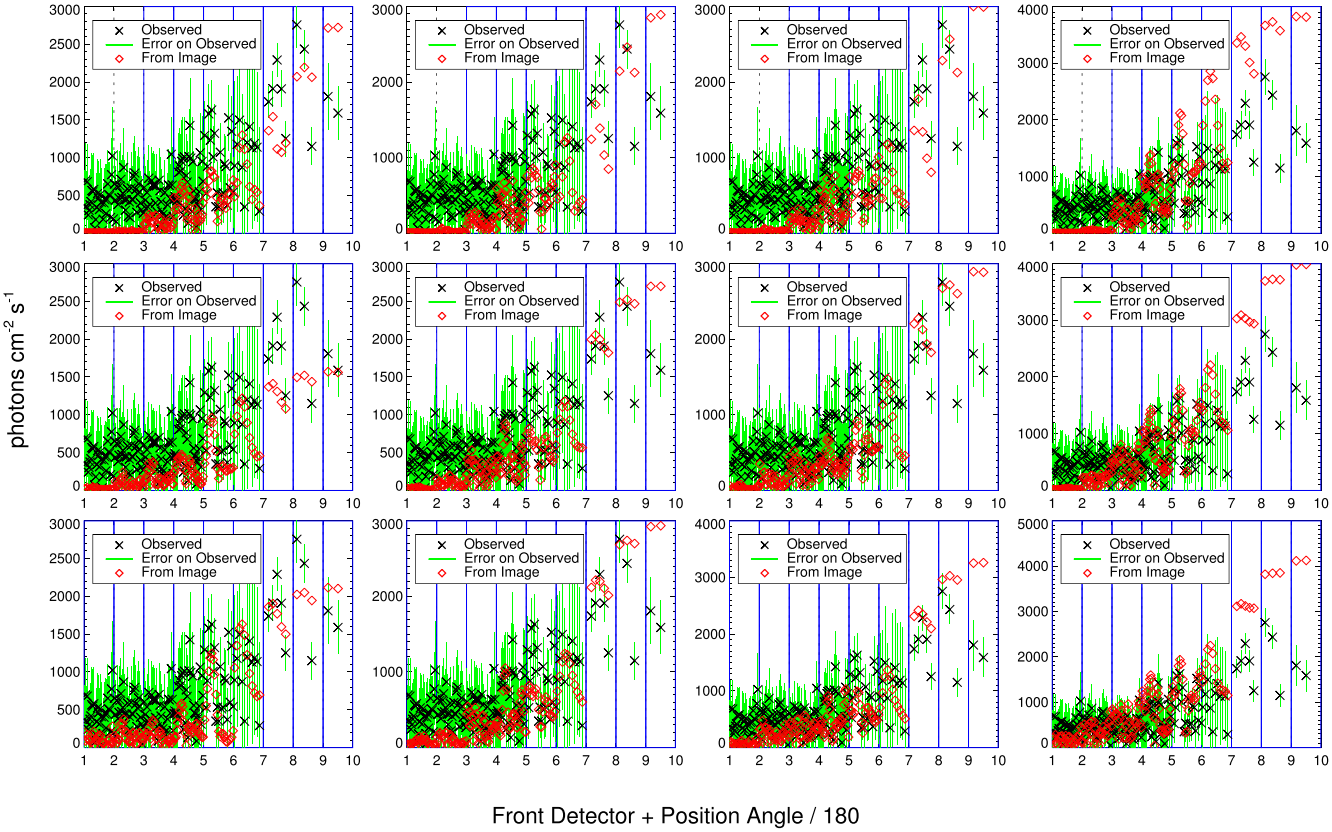

Figure 7. Comparison between predicted and measured visibilities for the flare observed by RHESSI on 2014 May 3 at 16:07:04 UT. From left to right, the columns contain the fits corresponding to uv_smooth, uv_smooth_BP, uv_smooth_CC, and CLEAN. From top to bottom, the rows correspond to using detector configurations from 3 through 9, from 2 through 9, and from 1 through 9, respectively. The observed visibilities and associated error bars are represented by black crosses and green lines, respectively; the red diamonds denote the predicted visibilities.

Table 6
χ^2 Values Predicted by the Four Reconstruction Methods Applied to the RHESSI Visibilities Observed on 2014 May 3 at 16:07:04 UT

detectors	uv_smooth	uv_smooth_BP	uv_smooth_CC	CLEAN
3–9	1.04	0.99	1.01	2.78
2–9	0.93	0.91	0.91	2.03
1–9	0.76	0.94	1.08	1.93

Note. The values are computed with respect to the visibilities measured by detectors 3 through 9, 2 through 9, and 1 through 9, respectively.

motivated by accounting for peculiar aspects of the hard X-ray imaging problem from visibilities. In fact, on the one hand, the back-projected map is obtained by means of a straightforward linear approach, i.e., the direct computation of the discretized inverse Fourier transform, that does not introduce any constraint into the imaging process and therefore exploits just the experimental information provided by the measurements (all other improvements to image reconstruction do not share this linearity property). On the other hand, it is well established that a weakness of CLEAN is the fact that the determination of the reconstructed CLEAN map from the map of the CLEAN components is typically realized by means of convolution with an idealized point-spread function whose FWHM is chosen via totally heuristic considerations. Choosing ψ as the map of the CLEAN components is a way to exploit it in a completely objective way, within the framework of an automatic image reconstruction method.

In the following applications, the VSK-based algorithms that utilize the back-projected map and the map of the CLEAN components to construct the scaling function will be named uv_smooth_BP and uv_smooth_CC, respectively.

4. Applications to the Reconstruction of Flaring Sources

In this section we discuss the effectiveness of this enhanced release of uv_smooth for visibility-based image reconstruction by considering tests on both synthetic simulations obtained by means of the STIX simulation software and experimental RHESSI observations.

4.1. STIX-simulated Visibilities

We simulated four STIX configurations with an overall incident flux of 10^4 photons cm^{-2} s^{-1} (see Figure 2). The first two configurations (Configuration 1 and Configuration 2) consisted of two footpoints with centers located at two different positions along the main diagonal. The third and fourth configurations (Configuration 3 and Configuration 4) mimic two flaring loops, one at the center of the field of view and the other one off center (refer to Tables 1–4 for details on the parameters of the four considered configurations). For the 128×128 STIX reconstructed images, we fixed the pixel size as about $1'$, and the corresponding field of view in the (u, v) plane is about 0.16 arcsec^{-1}.

In order to empirically illustrate how the VSK bases work, we show in Figure 3 how the interpolation bases modify accordingly the function ψ for one of these configurations

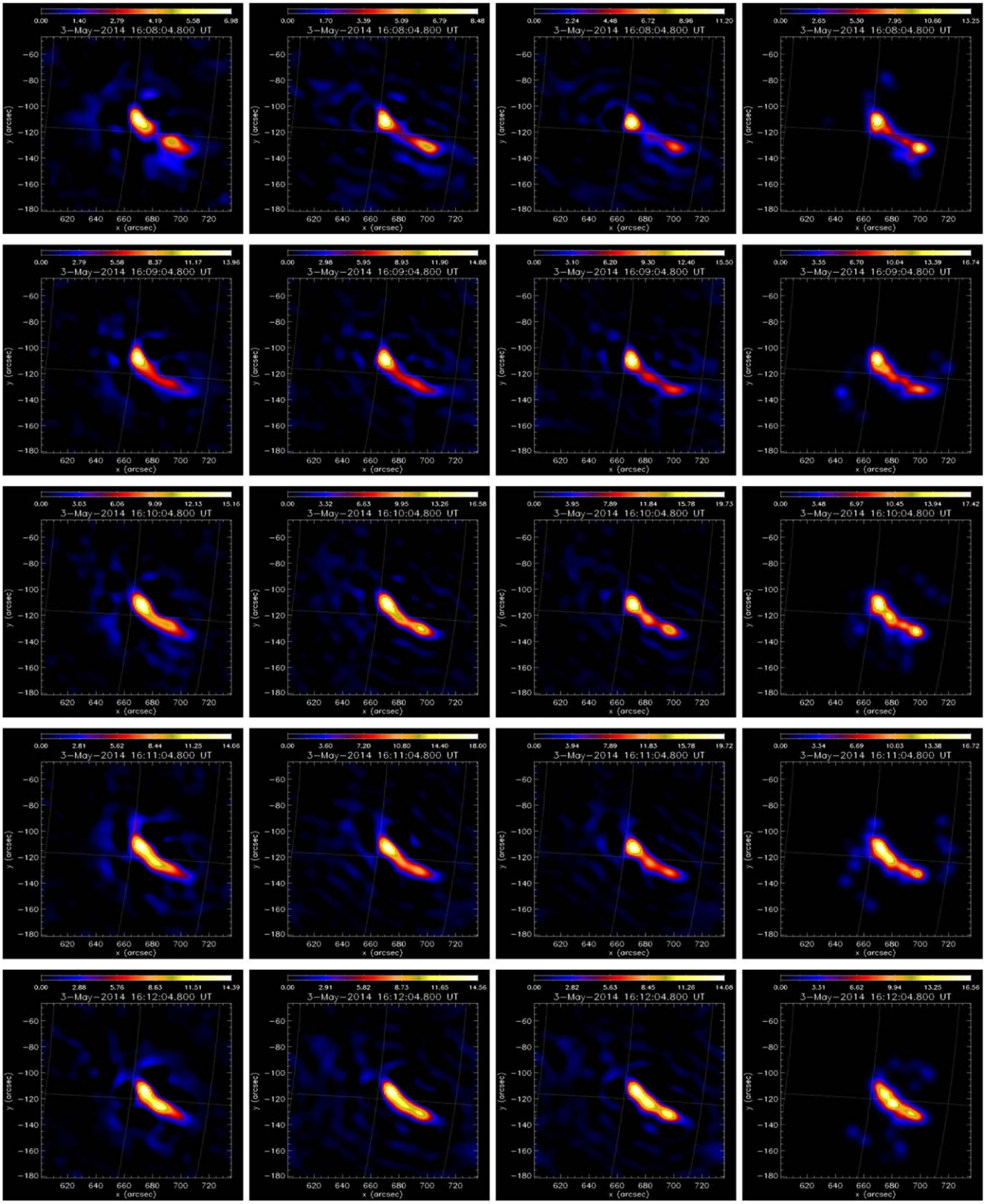

Figure 8. Reconstruction of the flare observed by RHESSI on 2014 May 3. From left to right, the columns contain the reconstructions obtained by uv_smooth, uv_smooth_BP, uv_smooth_CC and CLEAN. From top to bottom, the rows denote the evolution of the flare shape in five time intervals from 16:08:04 through 16:12:04 UT (integration time: 1 minute).

(Configuration 1). Specifically, in the left panel of the figure, we plot the contour levels of the modulus of the ground-truth visibility surfaces. Then, we show the contour levels corresponding to the reconstructions provided by uv_smooth_BP (middle panel) and the classical uv_smooth (right panel). In the middle and right panels, the corresponding basis

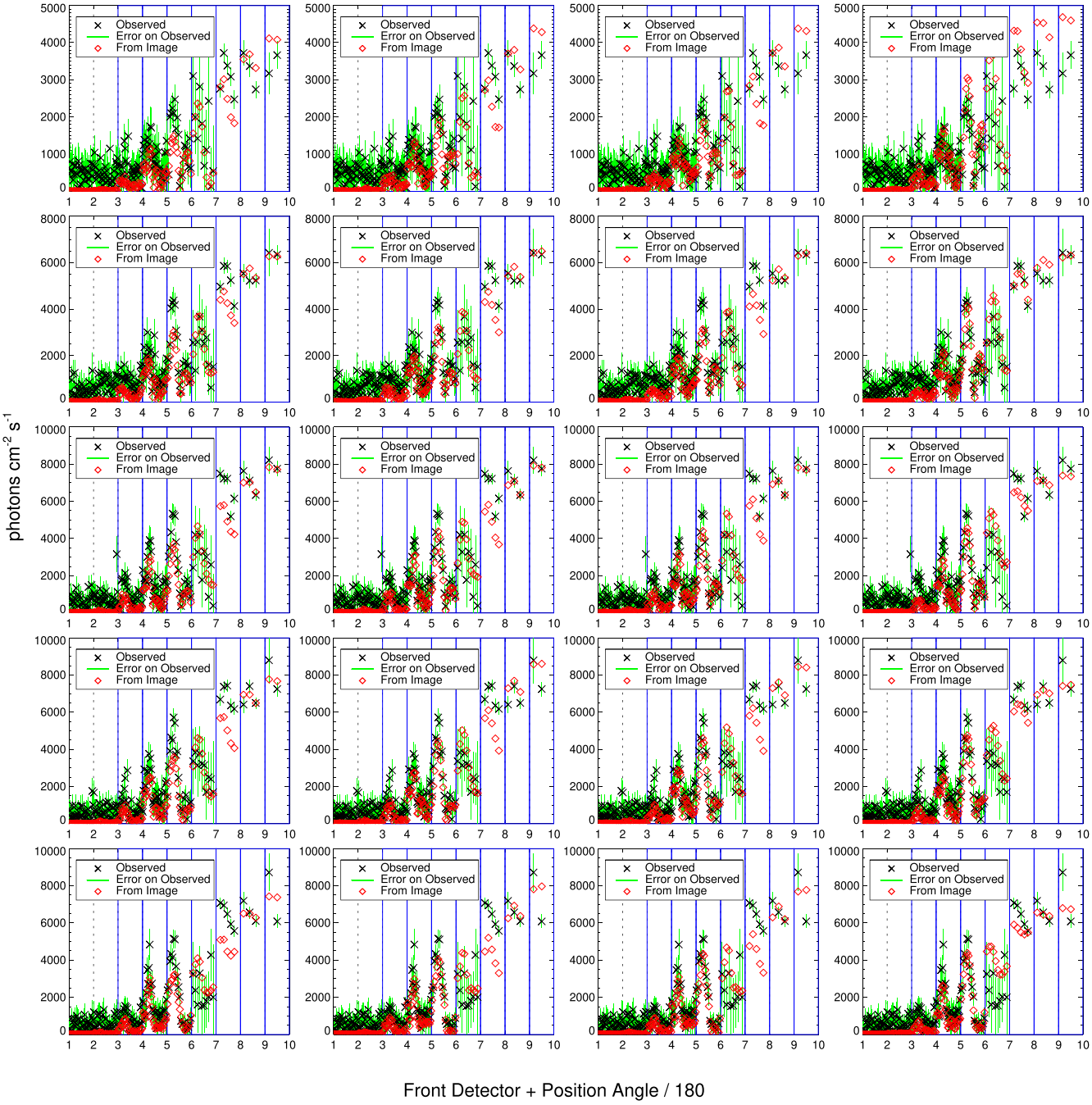

Figure 9. Comparison between predicted and measured visibilities for the flare observed by RHESSI on 2014 May 3. From left to right, the columns contain the fits corresponding to uv_smooth, uv_smooth_BP, uv_smooth_CC, and CLEAN. From top to bottom, the rows correspond to the evolution of the flare shape in five time intervals from 16:08:04 through 16:12:04 UT (integration time: 1 minute). The observed visibilities and associated error bars are represented by black crosses and green lines, respectively; the red diamonds denote the predicted visibilities.

functions are superimposed on the level curves. Overall, the figure clearly shows that the encoding of prior information on the solution into the VSK basis functions improves the reconstruction accuracy and forces the basis functions themselves to naturally adapt to the level curves.

In order to test the proposed imaging tool, using the STIX simulation software, we generated 25 synthetic realizations of the 60 STIX visibilities for each configuration. Then, Figure 4 shows the results provided by CLEAN, the original version of uv_smooth, uv_smooth_BP, and uv_smooth_CC. For the last two methods and throughout this subsection, the Tikhonov parameter for solving Equation (6) is set to zero. In Tables 1–4, the corresponding values of the reconstructed parameters are compared with the ones of the ground truths, where for each parameter we have given the average value with respect to the 25 realizations and the corresponding standard deviation. For the first and second configurations, we also show a comparison with a forward-fit scheme (see Figure 5 and Tables 1 and 2). Of course, the reconstructions are very accurate but this depends on the fact that we utilized for fitting the same Gaussian shapes utilized to generate the synthetic visibilities.

The CPU times employed to obtain the reconstructions are shown in Table 5. Tests have been carried out on an Intel(R) Core(TM) i7 CPU 4712MQ 2.13 GHz processor.

Table 7
χ^2 Values Predicted by the Four Reconstruction Methods Applied to the RHESSI Visibilities Observed on 2014 May 3 in the Five Time Intervals from 16:08:04 Through 16:12:04 UT (Integration Time: 1 Minute)

	uv_smooth	uv_smooth_BP	uv_smooth_CC	CLEAN
t_1	1.05	1.15	1.11	1.39
t_2	1.54	1.52	1.50	0.80
t_3	1.77	1.78	1.54	0.92
t_4	2.28	1.90	1.80	1.14
t_5	2.49	2.62	2.34	1.09

Note. The values are computed with respect to the visibilities measured by detectors 3 through 9.

Table 8
Total Fluxes Associated to the Reconstructions in Figure 8 Obtained by Means of the Four Reconstruction Methods Applied to the RHESSI Visibilities Observed on 2014 May 3 in the Five Time Intervals from 16:08:04 Through 16:12:04 UT (Integration Time: 1 minute)

	Total Flux ($\times 10^3$)			
	uv_smooth	uv_smooth_BP	uv_smooth_CC	CLEAN
t_1	4.85 ± 0.18	4.61 ± 0.14	4.87 ± 0.21	4.52 ± 0.19
t_2	6.74 ± 0.22	6.97 ± 0.15	6.87 ± 0.18	6.41 ± 0.14
t_3	8.32 ± 0.16	8.42 ± 0.21	8.36 ± 0.18	7.49 ± 0.21
t_4	8.23 ± 0.24	9.11 ± 0.31	9.03 ± 0.13	7.78 ± 0.25
t_5	7.98 ± 0.28	8.68 ± 0.26	8.45 ± 0.33	7.04 ± 0.31

Note. The values are computed with respect to the visibilities measured by detectors 3 through 9. The flux is measured as photons cm^{-2} s^{-1}.

4.2. RHESSI Observations

On Saturday, 2014 May 3 the GOES 1–8 Å passband instrument recorded nine C-class flares originating from three different active regions. In particular, in the time interval between 15:54:00 UT and 16:13:40 UT, RHESSI observed a C1.7 event whose flaring shape in the 3–6 keV energy channel evolved from a double footpoint to a narrow ribbon-like configuration. We have tested the effectiveness of this enhanced approach to interpolation in the (u, v) plane by considering five time intervals in that range, each one of 1 minute duration. First, we focused on the visibility bag recorded at 16:07:04 UT by the combination of RHESSI detectors 3 through 9 (212 visibilities), 2 through 9 (276 visibilities), and 1 through 9 (340 visibilities), respectively. Figures 6 and 7, respectively, compare the reconstructions and the corresponding visibility fitting provided by uv_smooth, uv_smooth_BP, and uv_smooth_CC with the reconstructions and the fitting given by CLEAN when the map of the CLEAN components is convolved a posteriori with an idealized PSF with a CLEAN beam-width factor equal to 2 (as done for the generation of the RHESSI image archive) and pixel dimension equal to about $1''$ in the 3 through 9 detector configuration and equal to about $0\farcs5$ for the other two combinations of detectors. For all images the number of pixels is 128×128; for detectors 3 through 9 the field of view in the (u, v) plane is about 0.16 $arcsec^{-1}$, while it is about 0.26 and 0.45 $arcsec^{-1}$ for detectors 2 through 9 and 1 through 9, respectively. As far as the Tikhonov parameter for solving Equation (6) is concerned, we fix it to zero for detectors 3 through 9, while for detectors 1 and 2 through 9, it is selected as $1/(S/N)$, where S/N is the signal-to-noise ratio of the visibilities.

The χ^2 values of the four reconstruction methods are reported in Table 6. Then, in Figures 8 and 9 we fixed the configuration based on detectors 3 through 9 and compared the reconstructions provided by the same four imaging methods as in Figure 6 and the corresponding fitting of the experimental measurements in the case of five time intervals between 16:08:04 and 16.12:04 UT. The χ^2 values predicted by the four reconstruction methods with respect to the observations are contained in Table 7. Finally, Table 8 contains the averaged fluxes and corresponding standard deviations associated with the reconstructions in Figure 8 and computed by running the four imaging methods on several randomly perturbed realizations of the input visibility bag.

5. Comments and Conclusions

Enhancing visibility interpolation is particularly crucial in the case of the STIX image reconstruction problem, where observations are linked to a set of 60 visibilities and, correspondingly, the sparsity of the sampling in the (u, v) plane is pronounced. As a confirmation of this, comparison with the four ground-truth configurations considered in the simulations of Figure 4 shows that the use of VSKs provides more accurate estimates of the imaging parameters; this is particularly true in the case of Configurations 2 and 4, which produce wilder oscillations in the visibility domain and where the need for powerful interpolation is more urgent. The computational times reported in Table 5 show that VSK interpolation increases the burden but keeps the reconstruction times competitive with the ones of most hard X-ray imaging methods.

In the case of RHESSI observations, the use of finer grids increases the spatial resolution but, at the same time, introduces high-resolution artifacts. However, also in this case we can notice an improvement brought by the use of VSKs with respect to standard uv_smooth, i.e., the progressive fragmentation of the reconstructed sources is less significant particularly when detectors 2 through 9 are used. For most cases, we notice that uv_smooth_BP and uv_smooth_CC can guarantee a nice tradeoff between reconstruction accuracy and fitting: imaging artifacts are less numerous and pronounced if compared to standard uv_smooth while χ^2 values are either comparable to or smaller than the ones corresponding to CLEAN reconstructions. These small χ^2 values can be explained within the regularization framework. In fact, the feature augmentation process realized by the introduction of the scaling function introduces a constraint on the characteristics of the source function we want to reconstruct and, therefore, a corresponding a priori bias on the possible physical interpretation of the results of the imaging process. However, the choices we made for ψ imply that the corresponding biases do not affect the ability of the reconstructed flaring sources to predict visibilities that nicely agree with the observed ones. Further, comparisons between uv_smooth_CC and CLEAN show that the former method can be interpreted as a user-independent way to exploit the CLEAN component map. Therefore, uv_smooth_CC concludes the overall CLEAN process, keeping the highly reliable step providing the CLEAN components and replacing the more heuristic one represented by the convolution with an idealized PSF with a totally automatic process based on feature augmentation.

Finally, as far as the physical interpretation of the results of the RHESSI data analysis is concerned, Figure 6 shows that, as

expected, the use of subcollimators characterized by finer grids implies an increase of the spatial resolution together with the presence of high-resolution artifacts, particularly in the region between the two footpoints. More interestingly, Figure 8 shows that this double footpoint configuration evolves with time to a ribbon-like shape, with a corresponding increase of the overall photon flux associated with the emission (see Table 8). This behavior is unusual but not a unicum in hard X-ray solar flare physics (Dennis & Tolbert 2019). One possible interpretation is that this shape is the result of low-lying loops extending from one footpoint to the other or that the plasma density in the corona is so high that the electrons deploy most of their energy there, before reaching the footpoints (Guo et al. 2013).

The authors acknowledge the financial contribution from the agreement ASI-INAF n.2018-16-HH.0. This research has been accomplished within Rete ITaliana di Approssimazione (RITA) and the UMI Group TAA Approximation Theory and Applications. This is the first paper that A.M.M. and M.P. submitted after Richard Schwartz passed away on 2020 December 12. In these difficult times for the whole of humanity, Richard's death has represented a further reason for sadness and grief for the RHESSI and STIX communities. A.M.M. and M.P. acknowledge that Richard's intellectual guidance is and will always remain an unforgettable source of inspiration for their current and future scientific activities.

References

Allavena, S., Piana, M., Benvenuto, F., & Massone, A. M. 2012, Inverse Probl. Imag, 6, 147
Aschwanden, M., Schmahl, E. & the RHESSI Team 2002, SoPh, 210, 193
Bigot, J., Boyer, C., & Weiss, P. 2016, IEEE Trans. Inf. Theory, 62, 2125
Bonettini, S., & Prato, M. 2014, InvPr, 30, 055004
Bozzini, M., Lenarduzzi, L., Rossini, M., & Schaback, R. 2015, IMA J. Numer. Anal, 35, 199
Brady, D. J., Choi, K., Marks, D. L., Horisaki, R., & Lim, S. 2009, OExpr, 17, 13040
Bronstein, M. M., Bronstein, A. M., Zibulevsky, M., & Azhari, H. 2002, IEEE Trans. Med. Imag, 21, 1395
Brossier, R., Operto, S., & Virieux, J. 2009, Geop, 74, WCC105
Campagna, R., & Perracchione, E. 2021, J. Sci. Comput., 88, 15
Caspi, A., Shih, A. Y., McTiernan, J. M., & Krucker, S. 2015, ApJL, 811, L1
Courrier, H. T., & Kankelborg, C. C. 2018, JATIS, 4, 018001
Culhane, J., Harra, L., James, A., et al. 2007, SoPh, 243, 19
Daubechies, I., Defrise, M., & De Mol, C. 2004, Commun. Pure Appl. Math., 57, 1413
De Marchi, S., Erb, W., Marchetti, F., Perracchione, E., & Rossini, M. 2020a, SIAM J. Sci. Comput, 42, B472
De Marchi, S., Marchetti, F., & Perracchione, E. 2020b, BIT Numer. Math., 60, 441
De Marchi, S., Schaback, R., & Wendland, H. 2005, Adv. Comput. Math., 23, 317
Dennis, B. R., & Tolbert, A. K. 2019, ApJ, 887, 131
Donoho, D. L. 2006, IEEE Trans. Inf. Theory, 52, 1289
Duval-Poo, M. A., Piana, M., & Massone, A. M. 2018, A&A, 615, A59
Eisebitt, S., Lüning, J., Schlotter, W. F., et al. 2004, Natur, 432, 885
Fasshauer, G. E. 2007, Meshfree Approximation Methods with MATLAB (Singapore: World Scientific)
Fasshauer, G. E., & McCourt, M. 2015, Kernel-based Approximation Methods Using MATLAB (Singapore: World Scientific)
Felix, S., Bolzern, R., & Battaglia, M. 2017, ApJ, 849, 10
Felli, M., & Spencer, R. E. 2012, Very Long Baseline Interferometry: Techniques and Applications, Vol. 283 (Berlin: Springer Science & Business Media)
Fessler, J. A. 2007, J. Magn. Reson., 188, 191
Fessler, J. A., & Sutton, B. P. 2003, ITSP, 51, 560
Gallagher, T. A., Nemeth, A. J., & Hacein-Bey, L. 2008, Am. J. Roentgenol, 190, 1396
Giordano, S., Pinamonti, N., Piana, M., & Massone, A. M. 2015, SIAM J. Imaging Sci, 8, 1315
Greengard, L., & Lee, J.-Y. 2004, SIAMR, 46, 443
Guo, J., Emslie, A. G., & Piana, M. 2013, ApJ, 766, 28
Harra, L. K., Hara, H., Doschek, G. A., et al. 2017, ApJ, 842, 58
Hurford, G., Schmahl, E., Schwartz, R., et al. 2002, SoPh, 210, 61
Jin, S. 2010, Geop, 75, WB103
Krucker, S., Hurford, G. J., Grimm, O., et al. 2020, A&A, 642, A15
Le Besnerais, G., Lacour, S., Mugnier, L. M., et al. 2008, ISTSP, 2, 767
Lee, J.-Y., & Greengard, L. 2005, J. Comput. Phys., 206, 1
Lin, R., Dennis, B., Hurford, G., et al. 2002, SoPh, 210, 3
Lustig, M., Donoho, D. L., Santos, J. M., & Pauly, J. M. 2008, ISPM, 25, 72
Marchesini, S., Boutet, S., Sakdinawat, A. E., et al. 2008, NaPho, 2, 560
Massa, P., Piana, M., Massone, A. M., & Benvenuto, F. 2019, A&A, 624, A130
Massa, P., Schwartz, R., Tolbert, A., et al. 2020, ApJ, 894, 46
Massone, A., Emslie, A., Hurford, G., et al. 2009, ApJ, 703, 2004
Massone, A. M., Piana, M., Conway, A., & Eves, B. 2003, A&A, 405, 325
Matérn, B. 1986, Lecture Notes in Statistics (Berlin: Springer-Verlag), 36
McGibney, G., Smith, M., Nichols, S., & Crawley, A. 1993, Magn. Reson. Med., 30, 51
Piana, M., & Bertero, M. 1996, JOSAA, 13, 1516
Piana, M., & Bertero, M. 1997, InvPr, 13, 441
Ravishankar, S., Ye, J. C., & Fessler, J. A. 2019, Proc. IEEE, 108, 86
Romani, L., Rossini, M., & Schenone, D. 2019, J. Comput. Appl. Math., 349, 532
Sciacchitano, F., Sorrentino, A., Emslie, A. G., Massone, A., & Piana, M. 2018, ApJ, 862, 68
Sutton, B. P., Noll, D. C., & Fessler, J. A. 2003, IEEE Trans. Med. Imag, 22, 178
Thiébaut, É., & Giovannelli, J.-F. 2009, IEEE Signal Process. Mag., 27, 97
Thompson, A., Moran, J., & Swenson, G. 2017, Interferometry and Synthesis in Radio Astronomy (Basingstoke: Springer Nature)
Wang, G., Ye, J. C., Mueller, K., & Fessler, J. A. 2018, IEEE Trans. Med. Imag, 37, 1289
Wiaux, Y., Jacques, L., Puy, G., Scaife, A. M., & Vandergheynst, P. 2009, MNRAS, 395, 1733
Winebarger, A. R., Weber, M., Bethge, C., et al. 2019, ApJ, 882, 12
Ye, H., Gull, S. F., Tan, S. M., & Nikolic, B. 2020, MNRAS, 491, 1146